Fermi National Accelerator Laboratory

FERMILAB-Conf-93/202-E

CDF

Direct Photon Results from CDF

The CDF Collaboration

Fermi National Accelerator Laboratory
P.O. Box 500, Batavia, Illinois 60510

August 1993

Submitted to the *International Symposium on Lepton and Photon Interactions*,
Cornell University, Ithaca, New York, August 10-15, 1993

Disclaimer

CDF/PUB/JET/PUBLIC/2159
FERMILAB-CONF-93/202-E

DIRECT PHOTON RESULTS FROM CDF

CDF Collaboration

Abstract

Results using isolated direct photons measured with the CDF detector during the 1992-93 run of the Fermilab Tevatron are presented. Photon detection and background subtraction are described. Measurement of the inclusive photon cross section as well as photon-jet cross sections are discussed and compared to next-to-leading order QCD predictions.

Submitted to International Symposium on Lepton and Photon Interactions,
Cornell University, Ithaca, NY, August 10-15, 1993

INTRODUCTION

Photons produced directly from the hard collision provide a probe of the gluon distribution function and an energy measurement which is free from the effects of fragmentation. This paper presents a brief summary of prompt photon results using the CDF detector[1] and data collected during the 1992-1993 running of the Fermilab proton-antiproton collider.

Photons are identified in the CDF detector by the presence of an isolated highly electromagnetic cluster which has no associated charged tracks[2, 3]. The main background is dijet events in which one of the jets has fragmented into a single π^0. While the probability for this fragmentation is quite low, the dijet cross section is much larger than the prompt photon cross section and at CDF energies the mix of signal to BKG is roughly 1:1.

A shower profile method and a conversion method are employed for separation of photons from the background. In particular, between 1989 and 1992 a new conversion detector was installed and has greatly improved photon-background separation at high P_T . In addition, an isolation requirement is now made at the low-level hardware trigger level. These improvements have resulted in increased statistics and better photon-background rejection than in 1989. The isolated inclusive photon cross section now spans over 6 orders of magnitude. The low x behavior of the gluon structure function is probed by measuring the photon-jet cross section.

PHOTON IDENTIFICATION

CDF has two statistical methods for separation of photons from the background. The shower profile method is based on the shower shape of the electromagnetic clusters as measured in the Central Electromagnetic Calorimeter Strip chambers (CES) which are embedded in the Central Electromagnetic Calorimeter (CEM) at approximately shower maximum (5.9 radiation lengths). The conversion method relies on the relative conversion probabilities of the photons and background. Between the 1989 and 1992 runs of the Tevatron, the Central PreRadiator multiwire proportional chambers (CPR) were installed outside the 1.09 radiation lengths of material in the CDF solenoid, just in front of the CEM calorimeter. Both the CES and CPR are shown in Figure 1.

The shower profile technique is described in detail in reference [2, 3]. The fundamental criteria is a χ^2 comparison of the shower shape as measured in the CES to that of single photons. While prompt photon events produce a χ^2 distribution which peaks below 4, π^0s produce a broad χ^2 distribution. The efficiency of a cut of $\chi^2 < 4.0$ is determined for true photons, ϵ_γ, and for the background, ϵ_B, as a function of P_T using Monte Carlo simulations

and test beam electrons. The fraction of photons is calculated using these efficiencies:

$$F_\gamma = \frac{\epsilon_B - \epsilon}{\epsilon_B - \epsilon_\gamma},$$

where ϵ is the fraction of events in the data with $\chi^2 < 4$. Figure 2 shows the efficiencies for the shower profile method for the 1989 and 1992 data. This method can only be used for $P_T < 40$ GeV. As the P_T of the π^0 increases, the two clusters from the π^0 decay become indistinguishable.

The conversion method is roughly independent of P_T and thus allows measurement of the inclusive photon cross section over a wide P_T range. This method simply looks for the presence of hits in the CPR detector. Because a π^0 decays to two photons, it is more likely to produce a conversion which will be measured in the CPR. Figure 2 also shows the conversion probability for photons and π^0's as predicted by the Monte Carlo and as measured in the data. Note that the curves are flat above P_T =25 GeV (which will lead to a measurement that is almost independent of P_T) and that the P_T range shown for this data extends to 120 GeV.

TRIGGER and DATA SAMPLE

The bulk of the photon data has been collected using thresholds on the photon P_T of 6 (prescaled by 300) and 16 GeV (unprescaled), and a trigger which makes a loose isolation requirement. For high P_T photons, a threshold of P_T >50 GeV is used and no isolation requirements are made.

In the offline analysis, an isolation requirement of < 2 GeV in a cone of radius 0.7 around the photon is made. The data analysis cuts are identical to the cuts described in reference [2, 3] with the exception of the no charged track requirement which now extends to a slightly wider range in rapidity. The total integrated luminosity is $\approx 10/300 = 0.03 pb^{-1}$ below a P_T of 16 GeV; $\approx 10 pb^{-1}$ for P_T of 16-70 GeV; and $\approx 18 pb^{-1}$ for P_T above 70 GeV.

INCLUSIVE PHOTON CROSS SECTION

The inclusive photon cross section has been measured using both the shower profile method and the conversion method. Both cross sections are shown in Figure 3, as well as the 1988-1989 cross section. All three are in good agreement, even though statistical uncertainties only are shown. Note that the new measurement now extends from 8 GeV to 120 GeV in P_T .

The systematic uncertainties on the profile method are mainly due to uncertainties in the shower shape and profile, and are discussed in detail in [2, 3]. The systematic uncertainties

in the conversion method are mainly due to the single photon conversion probability. This includes the true pair production cross section for the materials in the CDF solenoid magnet, the amount of material in the magnet, the number of conversions from the underlying event, and dead detector channels. We now discuss how we can calibrate all of these effects at once, using reconstructed meson peaks.

CDF can reconstruct η and π^0 mesons by searching for photons in separate calorimeter towers at low P_T where the two photons from the mesons are well separated. The method is described in detail in [2, 3]. The two-photon mass distribution is shown in Figure 4, displaying clear meson peaks. We can then check the CPR hit efficiency by plotting this versus the two-photon mass in the region around the π^0, this is shown in Figure 5. We see that the measured CPR hit fraction in the π^0 peak region (after a sideband subtraction) is .852 $\pm$.01, and the expected efficiency is .848, in agreement to .004. Thus we could use .01 as the systematic uncertainty on the CPR hit rate, this would lead to a 6-12% cross section uncertainty, which is the goal for 1992-93. But there is an unexplained structure inside the π^0 peak region; the middle bin is significantly lower than the other two bins. Thus we take 0.02 as the systematic uncertainty on the CPR hit efficiency, which leads to cross section uncertainties of 12-24%.

Figure 6 shows the systematic uncertainties on the inclusive photon cross section due to the profile and conversion methods, and due to the photon energy scale and luminosity. Notice that below 15-20 GeV the uncertainties are growing rapidly on both background subtraction methods. This is due to a dramatic increase in the level of background for low P_T events. The profile method has smaller statistical uncertainties (not shown) and systematic uncertainties below 18 GeV, and the conversion method has much smaller uncertainties above 18 GeV. Therefore, in order to compare with theoretical predictions, we combine the profile and conversion methods. We use the profile method below 18 GeV and the conversion method above 18 GeV. Figure 7 shows the total systematic uncertainties after combination in quadrature.

Figure 8 shows the prompt photon cross section as measured by CDF using the 1992-93 data sample, compared to two next-to-leading order (NLO) QCD predictions. The predictions use the program of Baur et al.[4], and CTEQ parton distributions. There is a good qualitative agreement between data and theory, yet the data has a slightly different slope. This is seen better on a linear scale, as in Figure 9. Here we use as the default the parton distributions used in [2, 3]. You can see the data is much higher than the theory at low P_T

with these parton distributions, while the CTEQ parton distributions begin to reproduce the data better. This is due to the known changes in the deep inelastic scattering data at low x. Finally, Figure 10 displays the data versus the modern parton distribution, and three different choices of the renormalization scale. You can see that there is still a distinct slope difference between theory and data. The effect of higher order QCD effects, bremsstrahlung diagrams, and new gluon distributions are under study.

PHOTON-JET CROSS SECTION

The gluon distribution function is expected to dominate in low x interactions. The rapidities of the photon and jet are related to x by the equation:

$$x_{1(2)} = \frac{P_T}{\sqrt{s}}(e^{(-)\eta_{jet}} + e^{(-)\eta_\gamma})$$

For a central photon of P_T =7 GeV and a central jet , $x_1 = x_2 \approx 0.008$, while for a central photon and a jet in the range $1.4 < |\eta_{jet}| < 2.2$, $x_1 \approx 0.02$ and $x_2 \approx 0.004$. By measuring the cross section for different photon and jet rapidities, a wide range of x can be probed.

Questions arise about the measurement of low energy jets at a hadron collider, in the presence of an underlying event. In Figure 11 we show four plots demonstrating the quality of the jets in our lowest P_T bin. The upper left plot shows the P_T spectra of the jet and photon. As expected, the jet has a worse resolution than the photon, but the mean values of the distributions are similar. The upper right plot displays the fractional P_T difference between the jet and the photon, showing they balance in P_T on average. The lower left plot shows that the photon and jet are back-to-back in ϕ, which would not be true if a random energy deposition were being used. Finally, the lower right plot is an $\eta - \phi$ scatter plot of the jet being used, detector problems would show up on this plot as spikes, none are seen.

Figure 12 shows the inclusive photon cross section, with no additional jet cuts, and the cross section for a photon in the central region ($|\eta_\gamma| < 0.9$) and a jet in the endplug detector ($1.4 < |\eta_{jet}| < 2.2$). In all cases the photon will be constrained to the central detector. Both agree well with NLO QCD predictions, the prediction with the older parton distribution (HMRS E+) is disfavored. We now plot the ratios of cross sections, in order to reduce the experimental and theoretical uncertainties. Figure 13 shows the ratio of the photon-jet cross sections for the case where the jet is restricted to the endplug region $1.4 < |\eta_{jet}| < 2.2$ to the case where the jet is restricted to the central region $|\eta_{jet}| < 0.9$. Theoretical predictions for three sets of parton distribution functions are again shown, and there is good qualitative agreement with the more modern parton distributions, but the data tend to fall below the

predictions. Finally, Figure 14 shows the ratio of cross sections for the case when the photon and jet are on the same side of the detector in η, to the case when the photon and jet are on opposite sides of the detector in η. In both cases the jet is in the endplug region described above. Once again there is good qualitative agreement with the more modern parton distributions.

CONCLUSIONS

With about half of the data of the 1992-93 run analyzed, CDF has already been able to investigate the low x behavior of the parton distributions, and to greatly extend the P_T range and statistics of the inclusive photon cross section measurement.

References

[1] F. Abe et al. (CDF Collaboration), *Nucl. Instr. Meth.* A271, pp.387, (1988).

[2] F. Abe et al. (CDF Collaboration), *Physical Review Letters*, 68:2734, 1992

[3] F. Abe et al. (CDF Collaboration), Submitted to Phys., Rev. D.;ANL-HEP-PR-93-09.

[4] J. Ohnemus, H. Baer and J.F. Owens., *Physical Review D*, 42(1):61, 1990

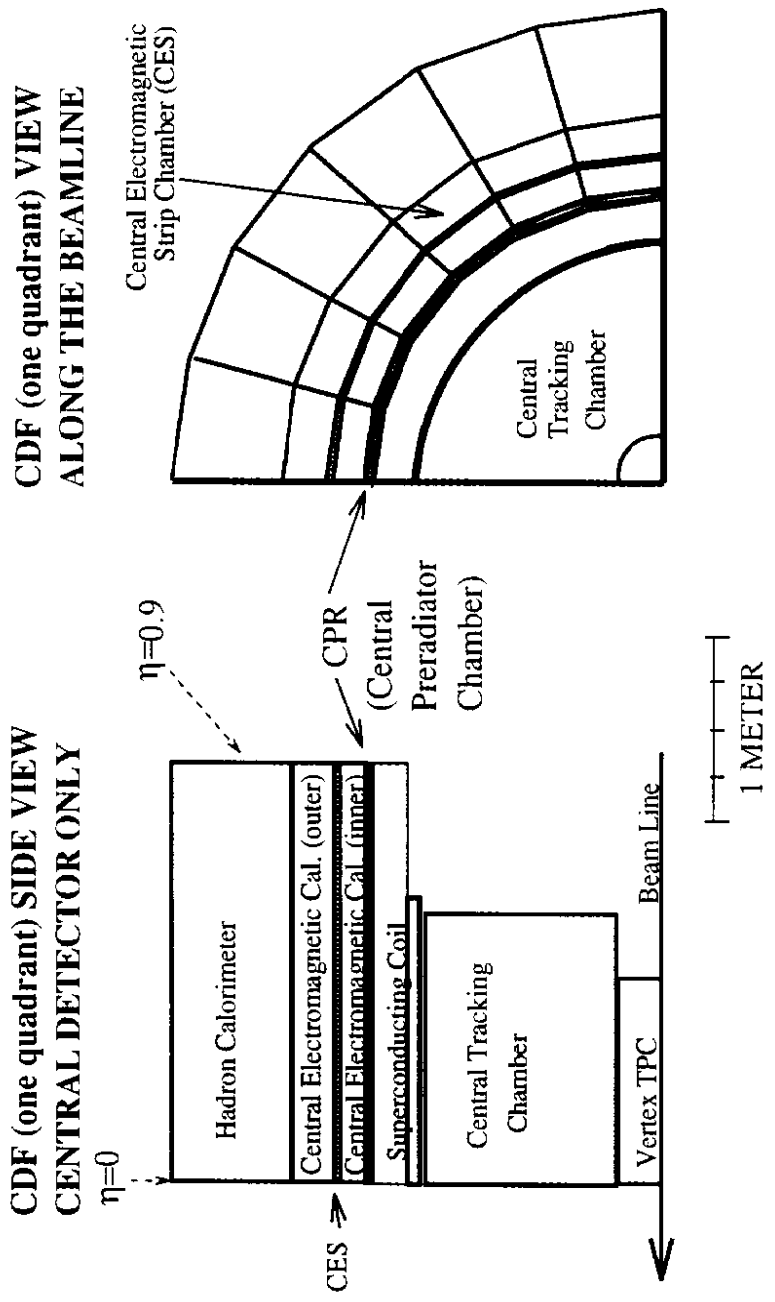

Figure 1: The upgraded CDF central detector, showing the new Central PreRadiator (CPR) detector and the shower maximum detector (CES).

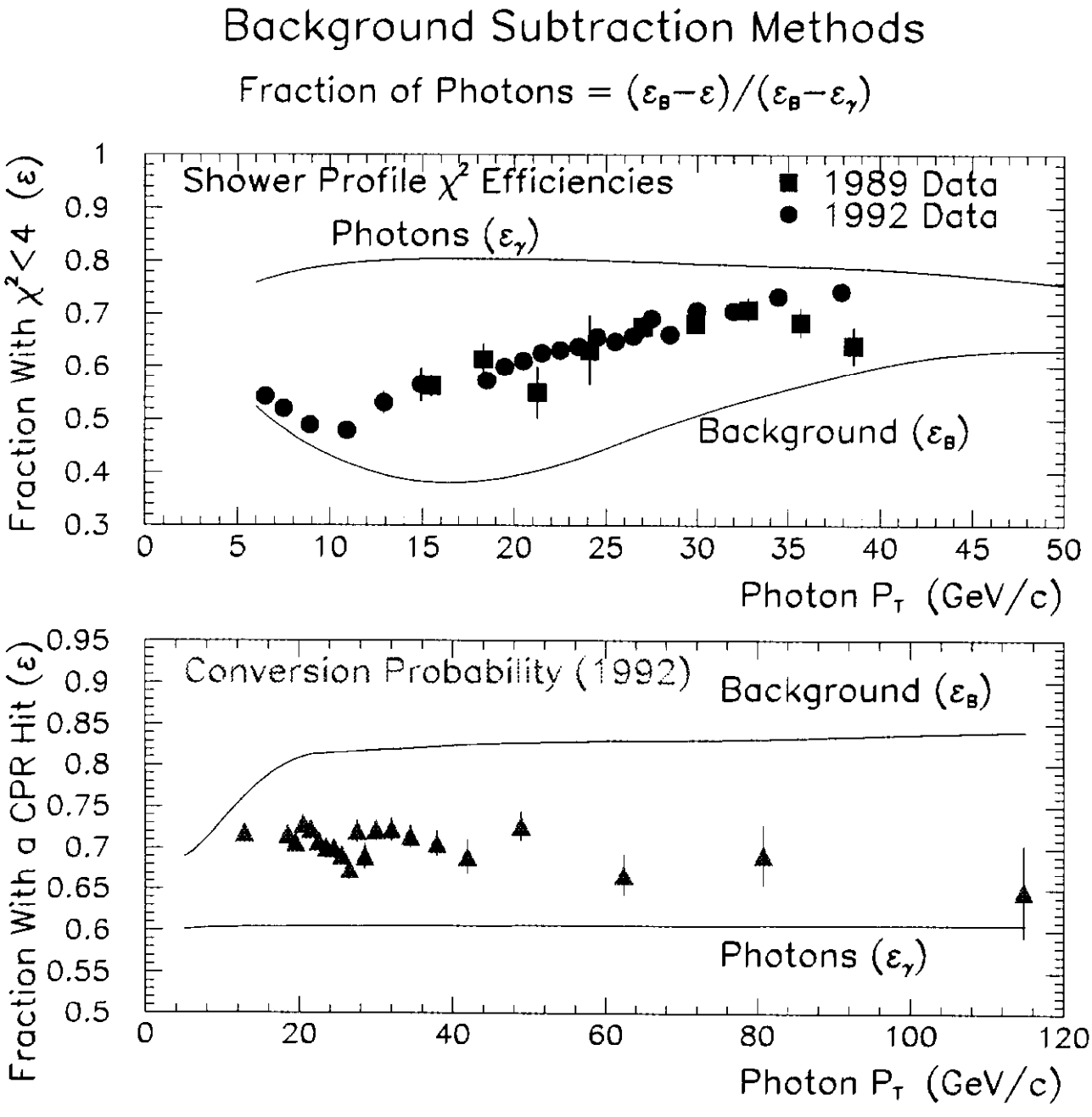

Figure 2: The CDF direct photon background subtraction techniques, the shower profile method and the conversion method. Shown are the data points and the predicted curves for single photons and backgrounds.

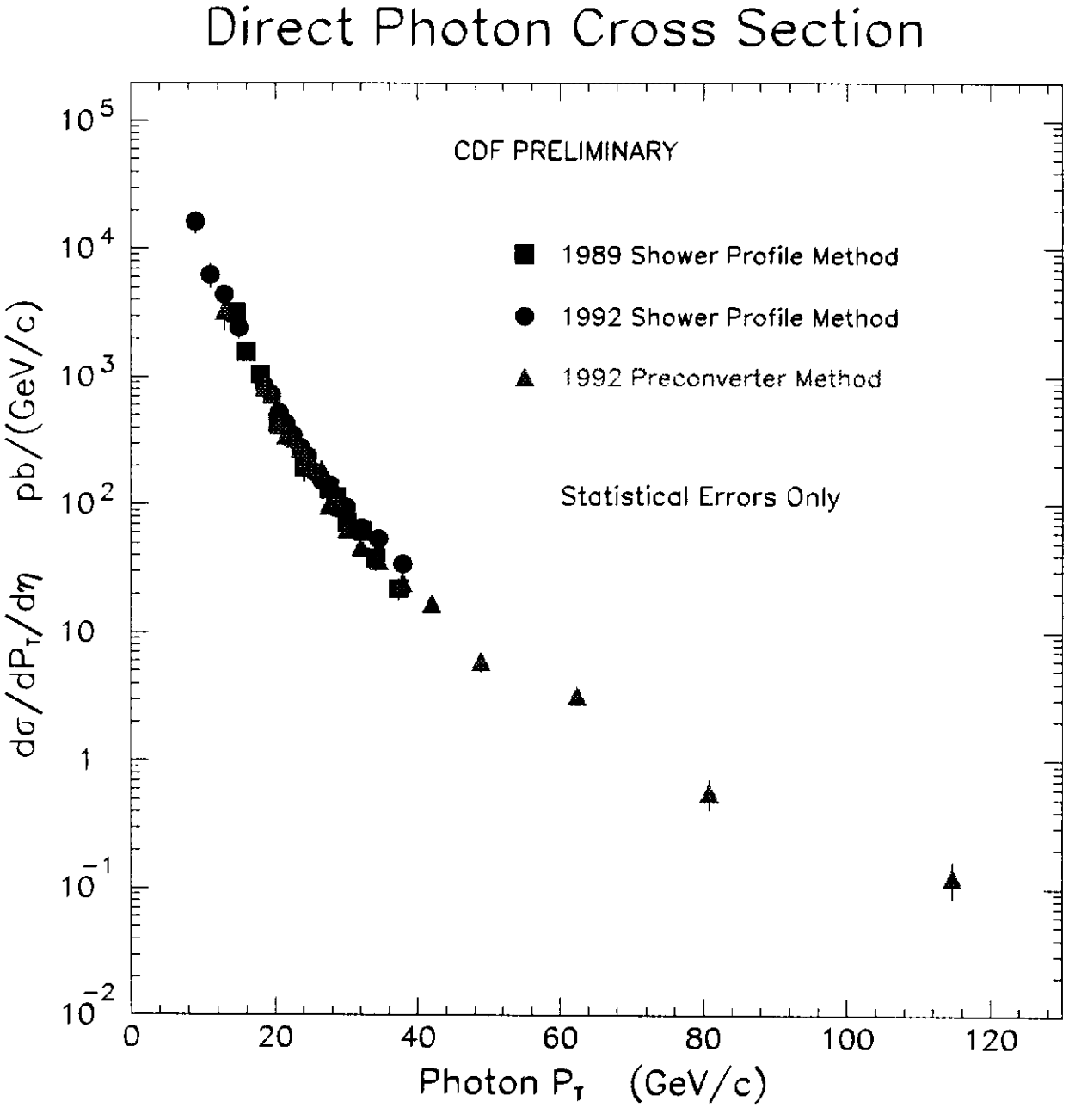

Figure 3: The 1992 photon cross sections as measured by both the profile and conversion methods. Also shown is the final 1989 cross section.

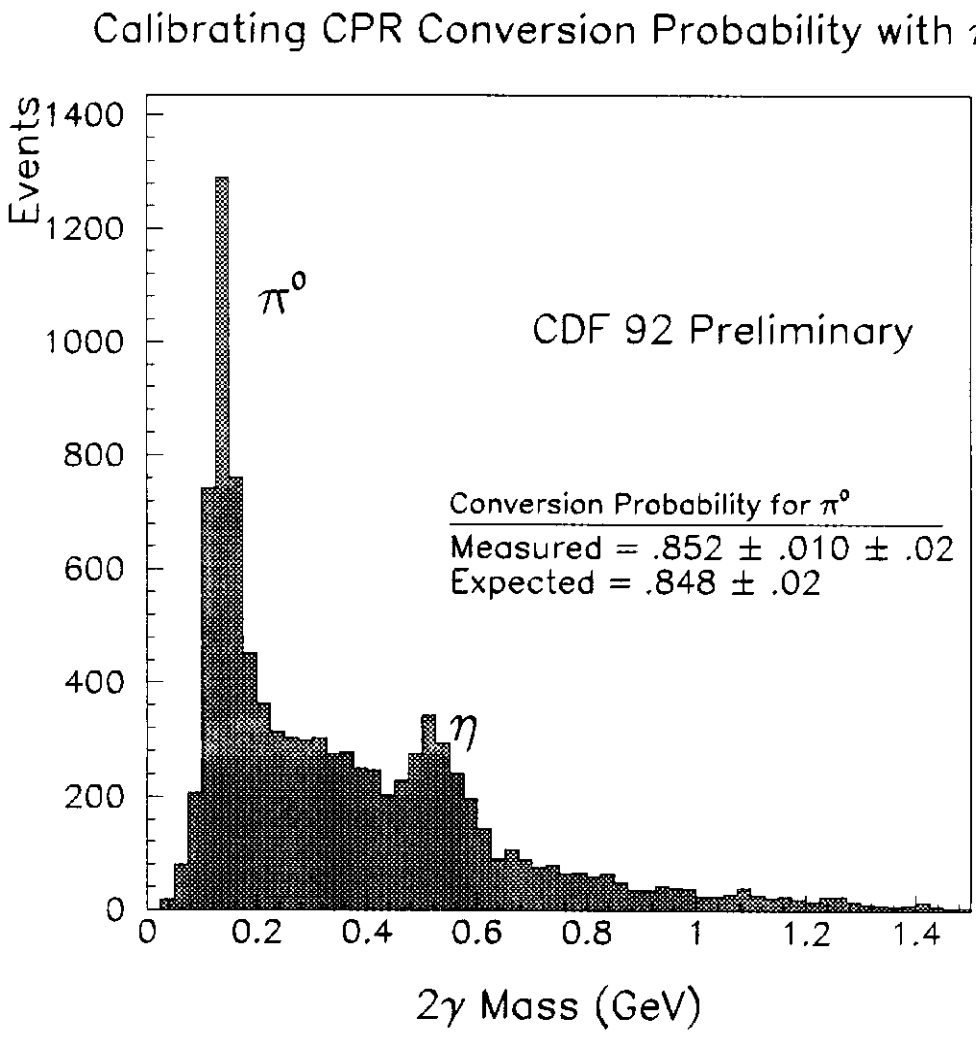

Figure 4: Two-photon mass distribution, showing clear π^0 and η meson peaks.

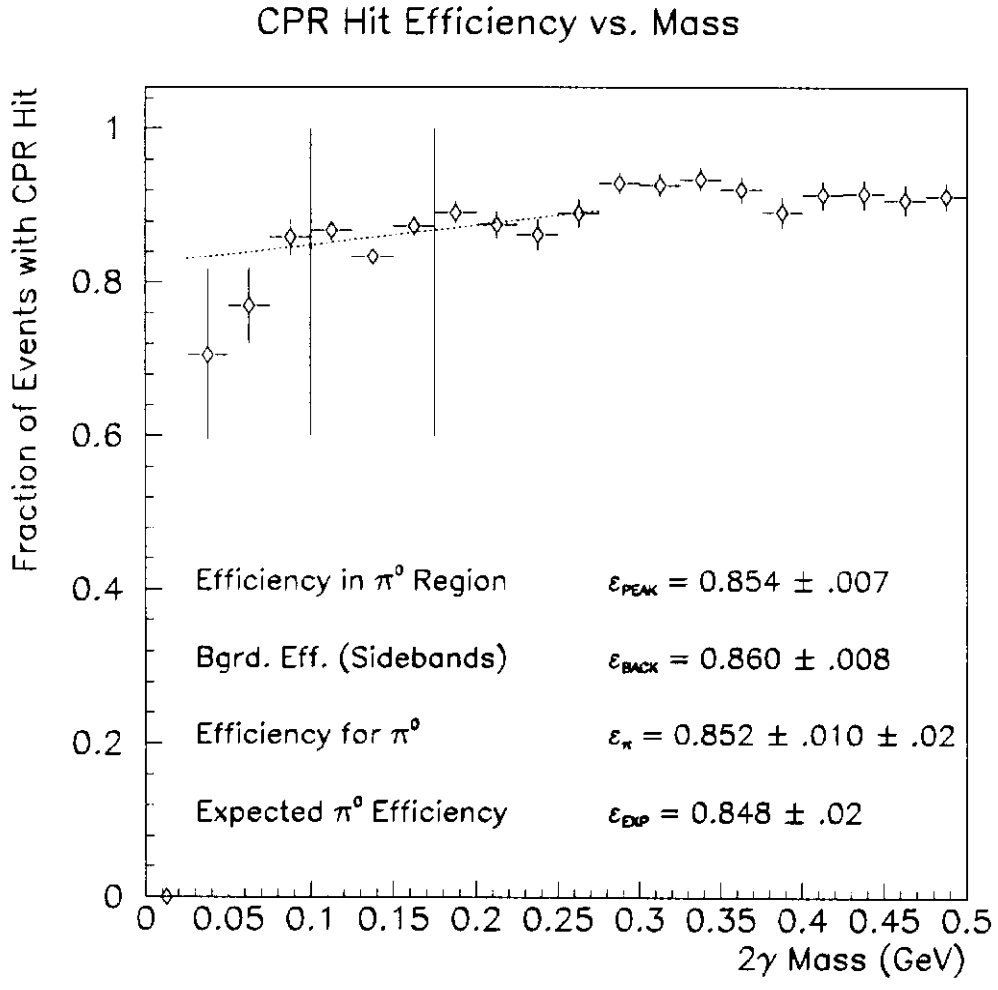

Figure 5: The CPR hit efficiency versus the two-photon mass. This shows the hit efficiency in the π^0 region and the adjacent regions that are used in a sideband subtraction.

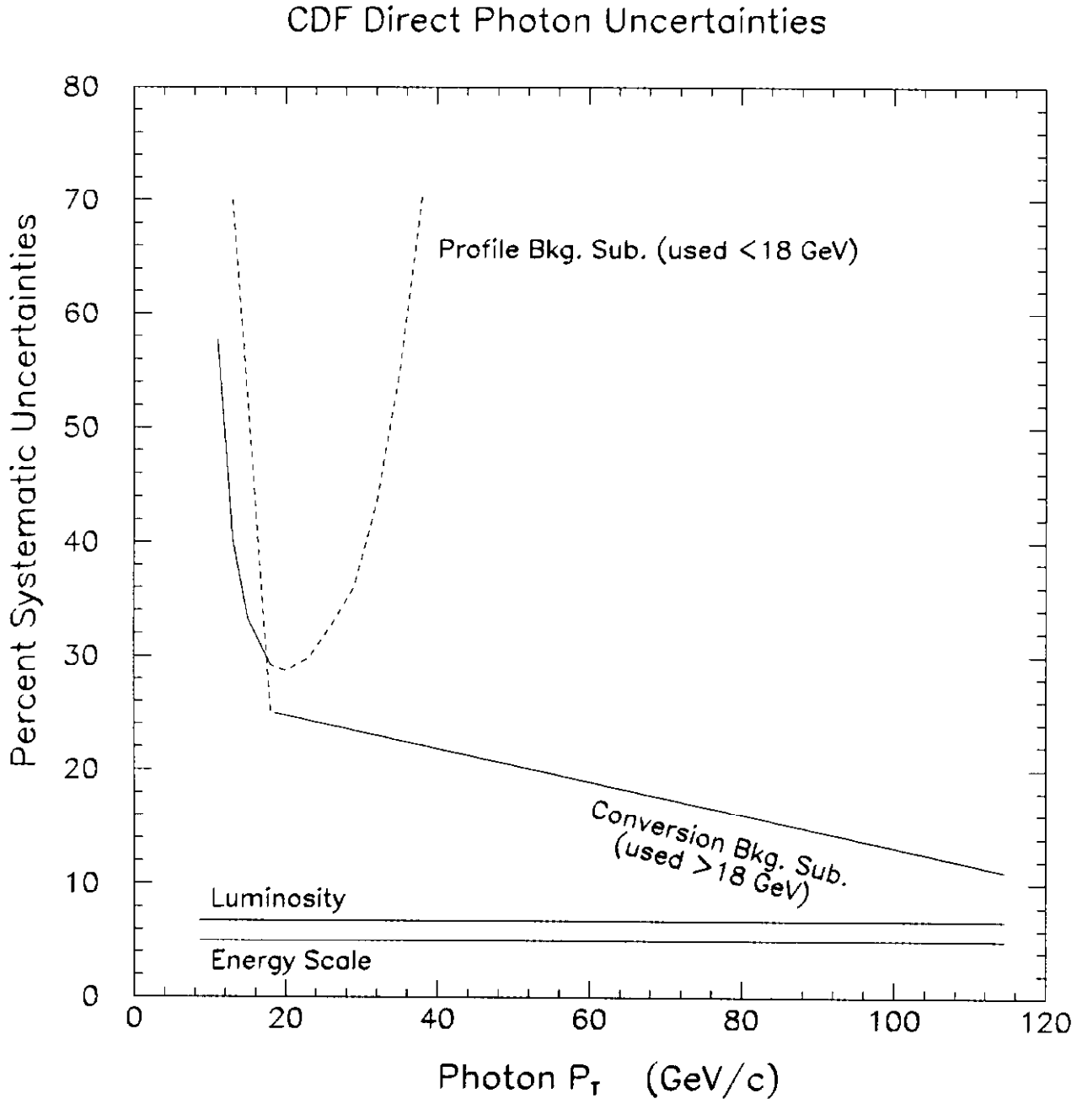

Figure 6: Systematic uncertainties in the CDF direct photon cross section.

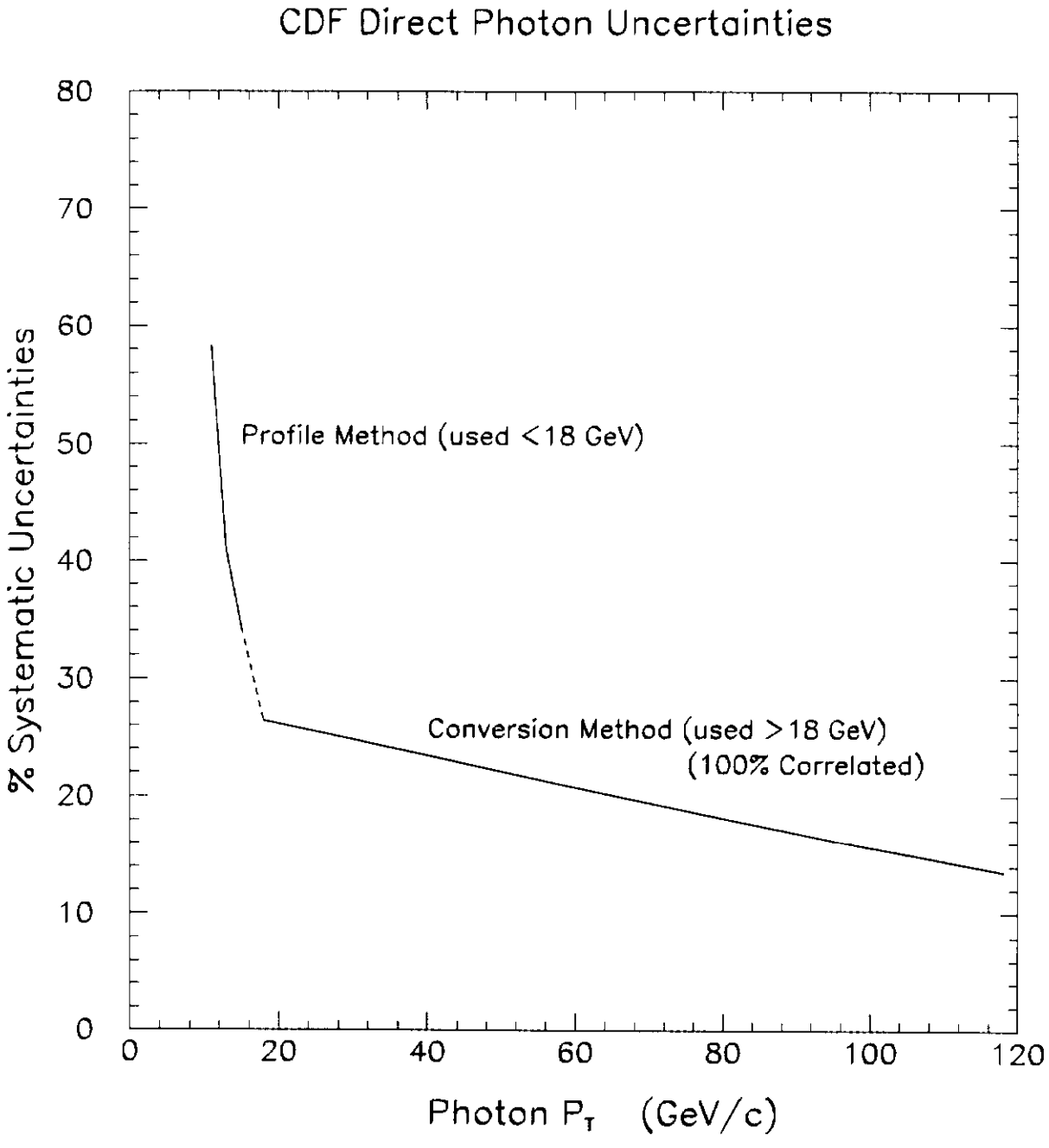

Figure 7: The total combined systematic uncertainty in the CDF direct photon cross section.

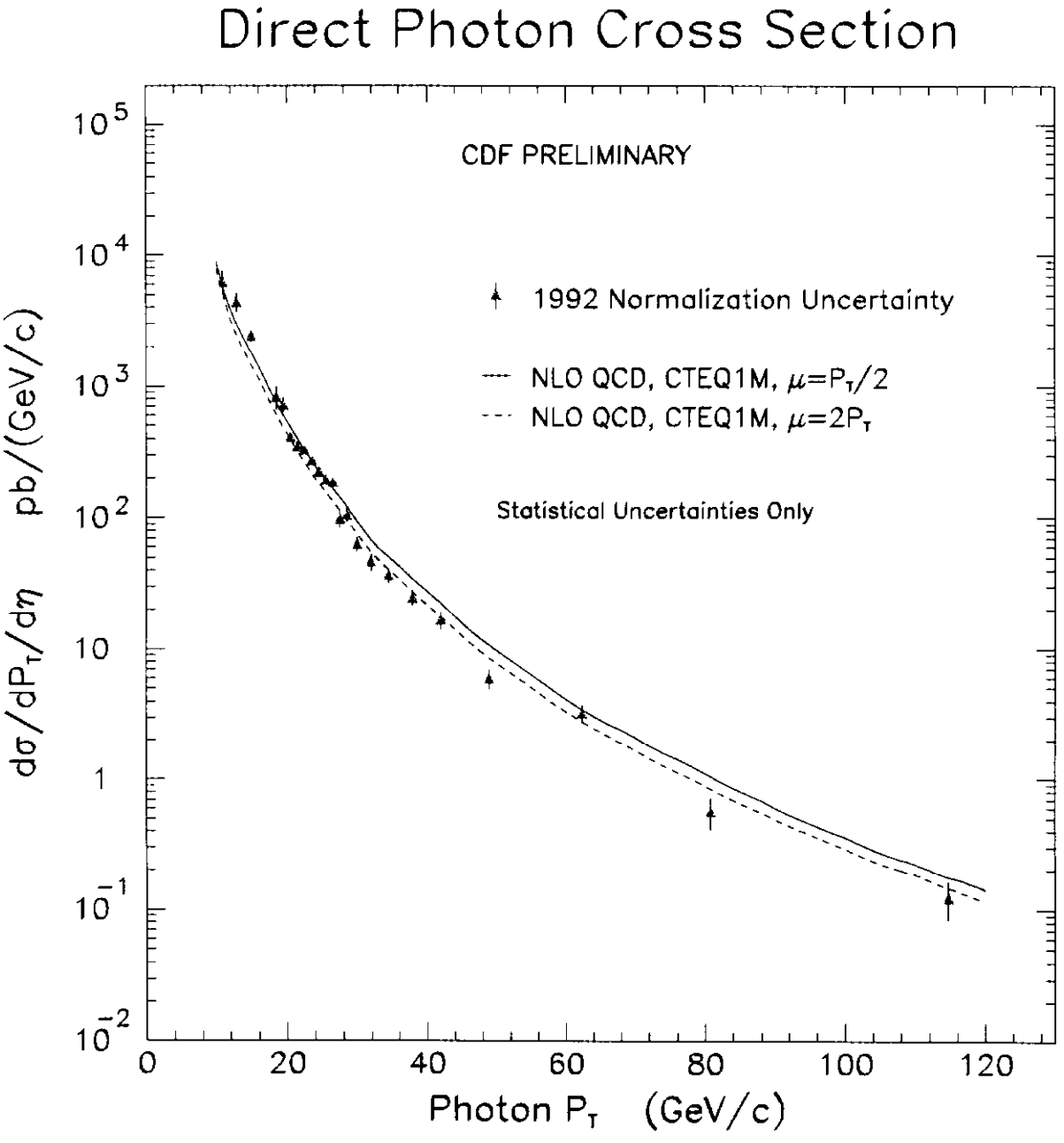

Figure 8: The CDF inclusive isolated photon cross section compared to NLO QCD predictions.

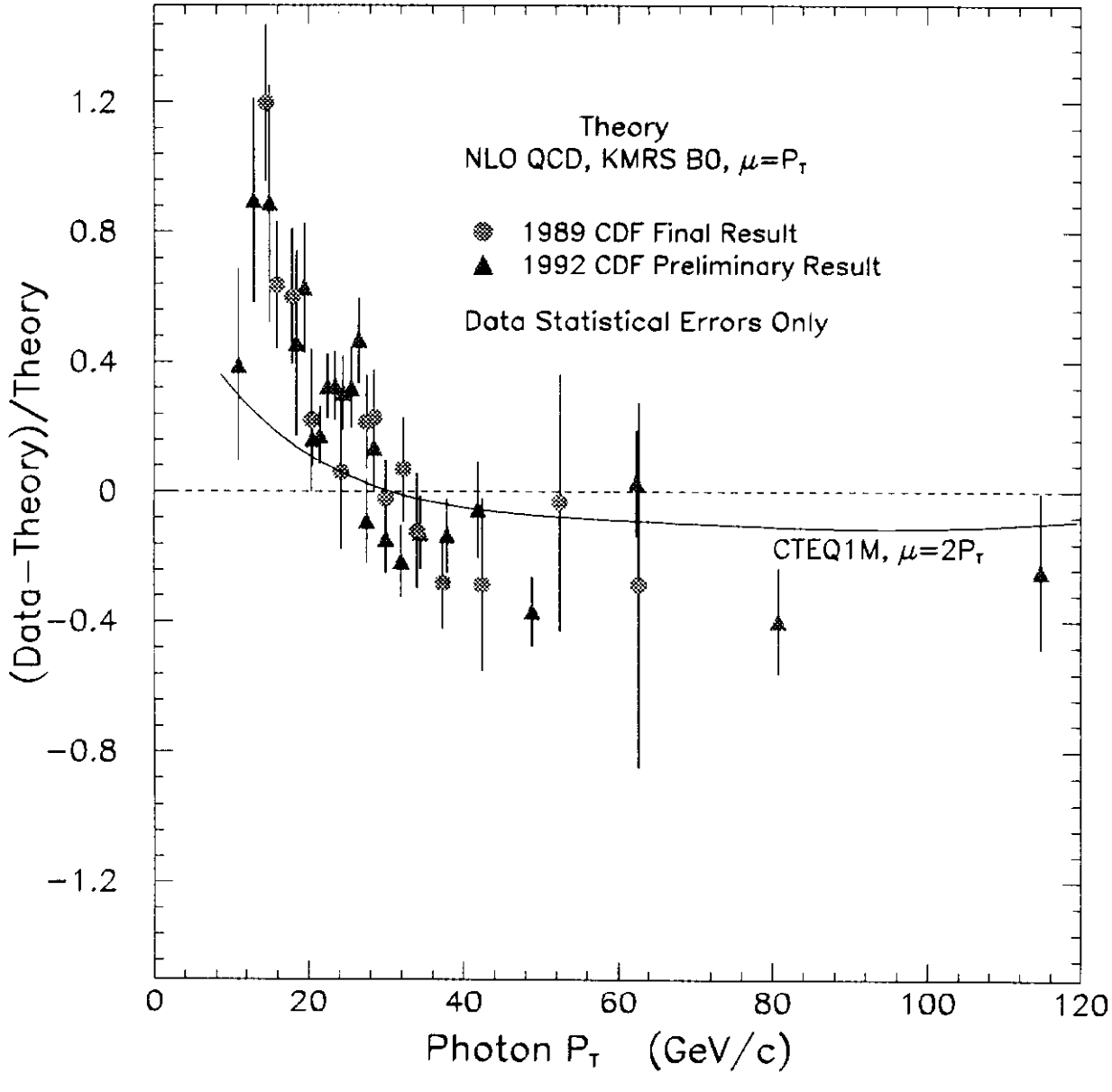

Figure 9: The CDF inclusive isolated photon cross section compared to NLO QCD predictions. The default theory uses older parton distributions, while the line represents a more modern version. The effect of the parton distributions is evident on the shape of the cross section.

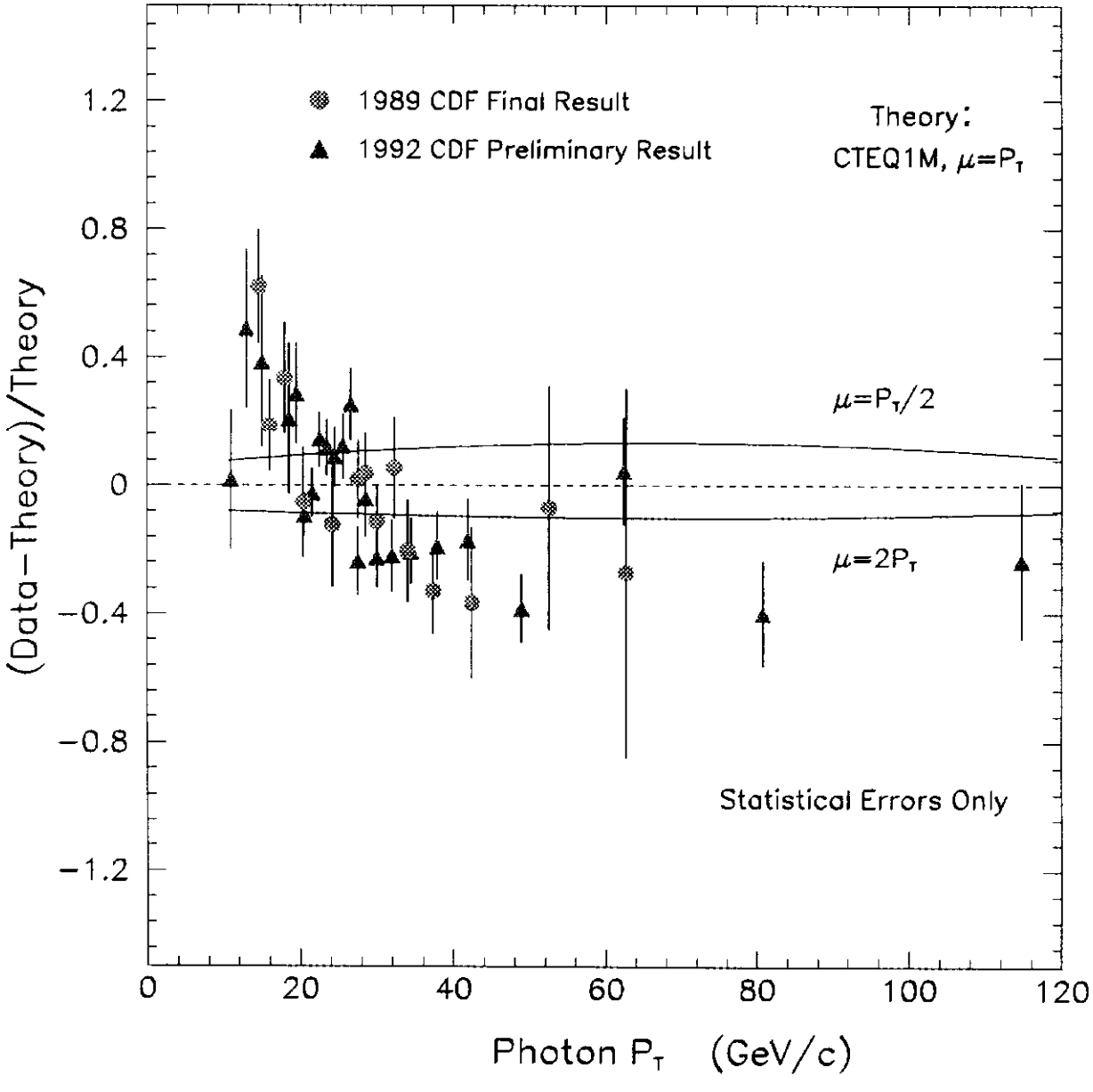

Figure 10: The CDF inclusive isolated photon cross section compared to NLO QCD predictions. Modern parton distributions are used, and the renormalization scale in the theory is varied.

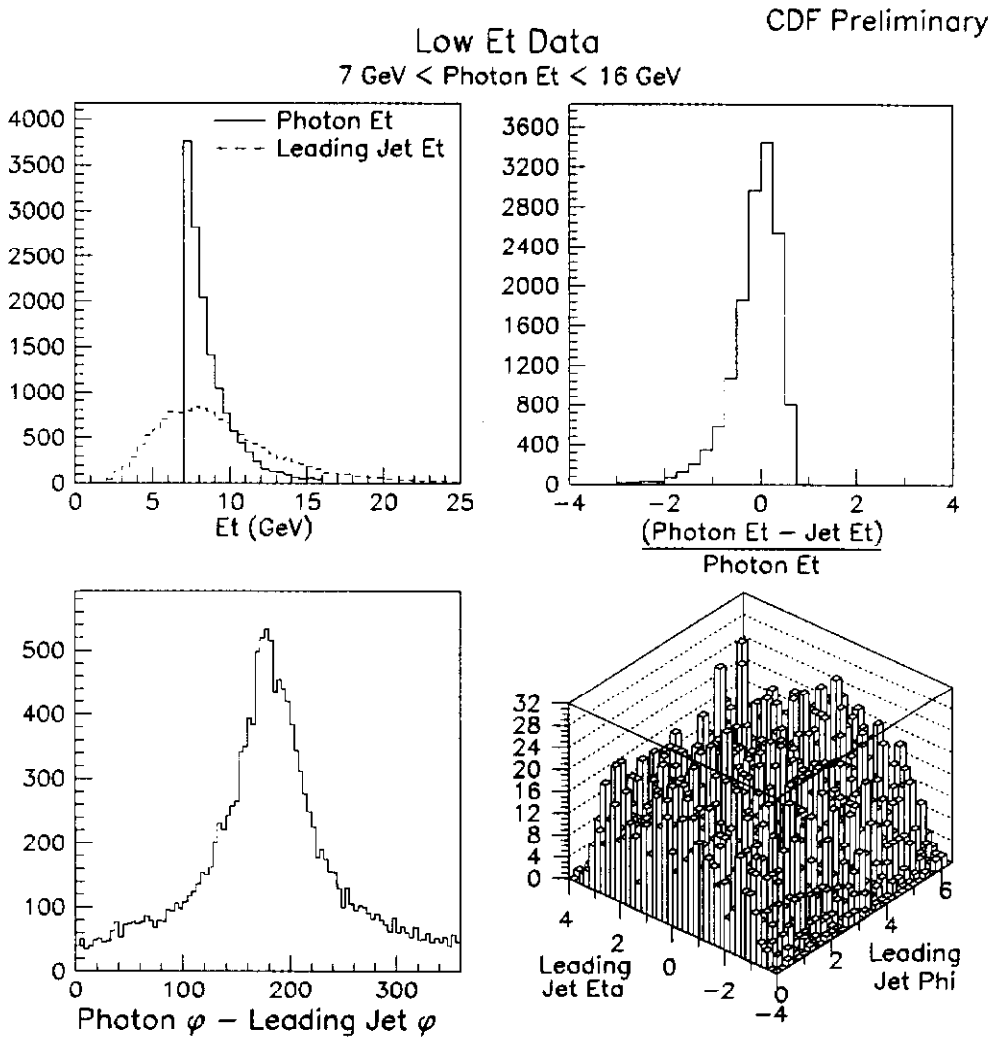

Figure 11: The quality of the low energy jets used in photon-jet kinematics studies is shown.

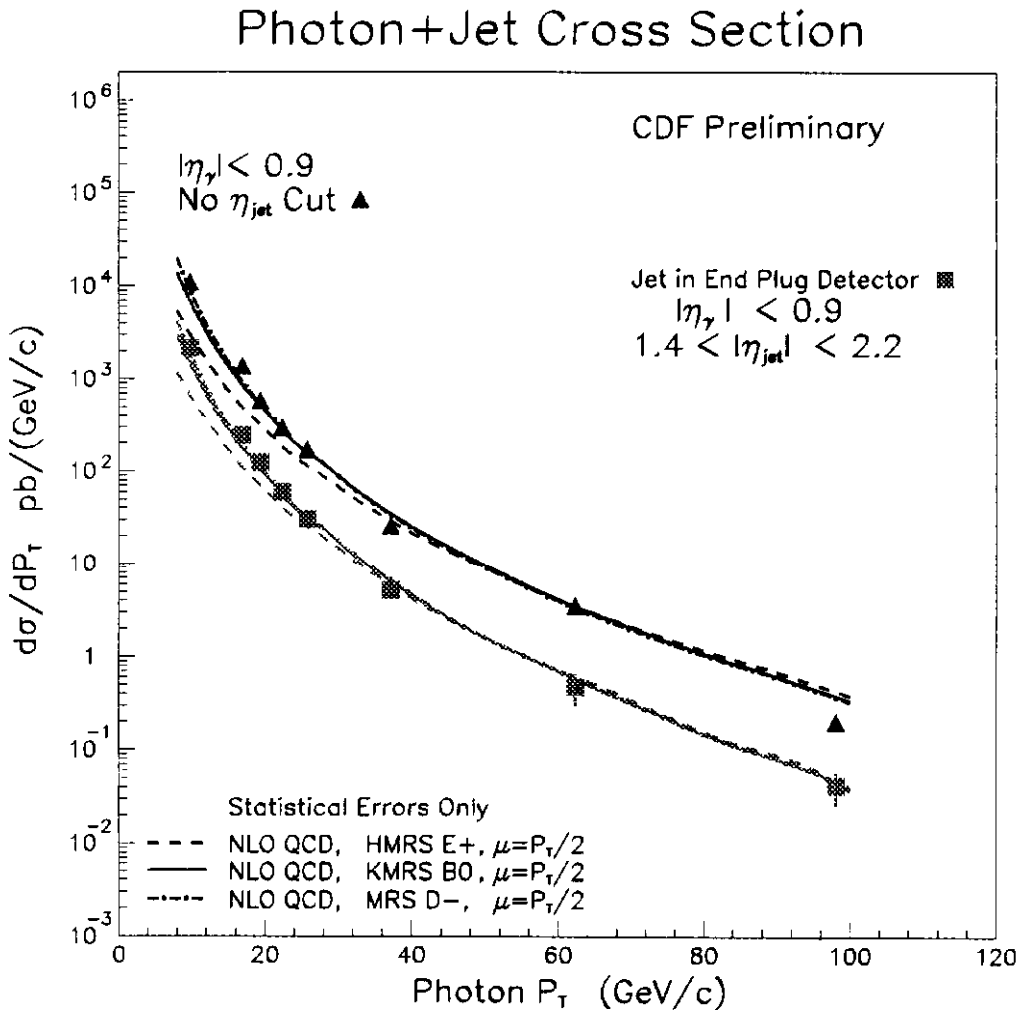

Figure 12: The inclusive photon cross section is compared to the cross section with a jet in the endplug detector. Both are compared to NLO QCD predictions. The exact cuts are described in the text.

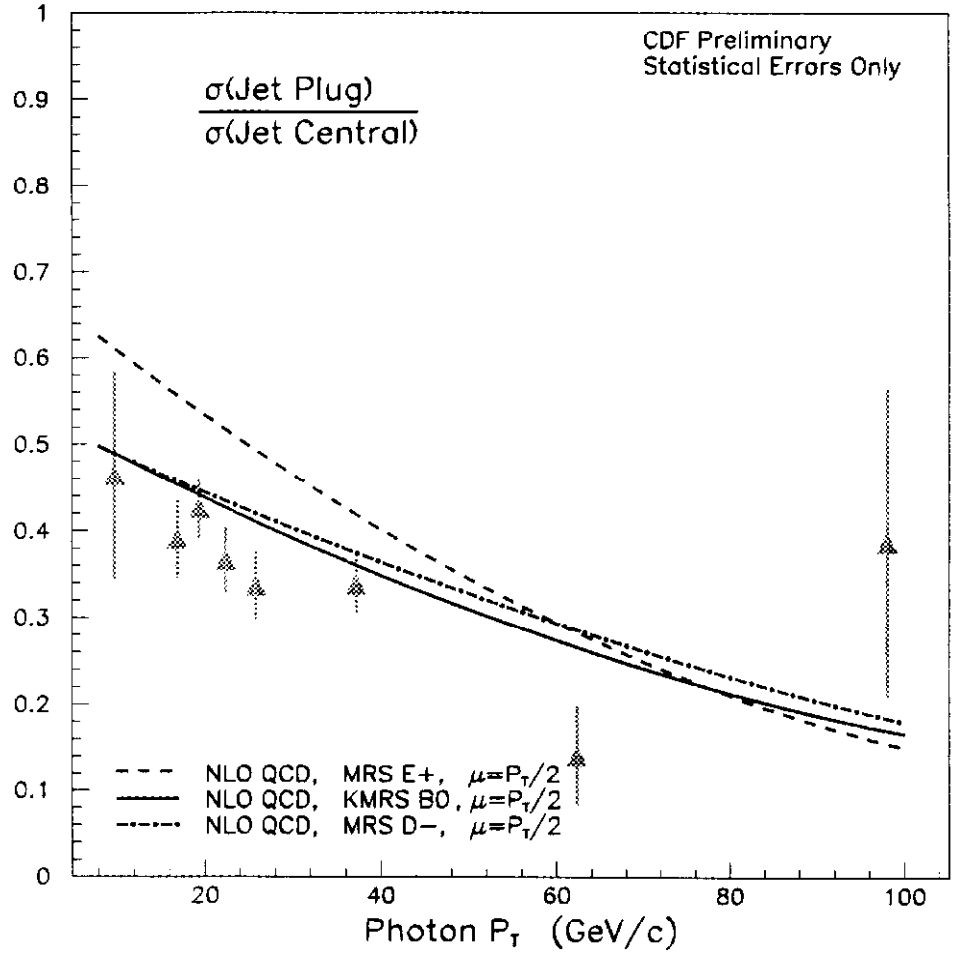

Figure 13: The ratio of two photon+jet cross sections is shown. This is the ratio of the case when the jet is in the endplug detector to the case when the jet is in the central detector.

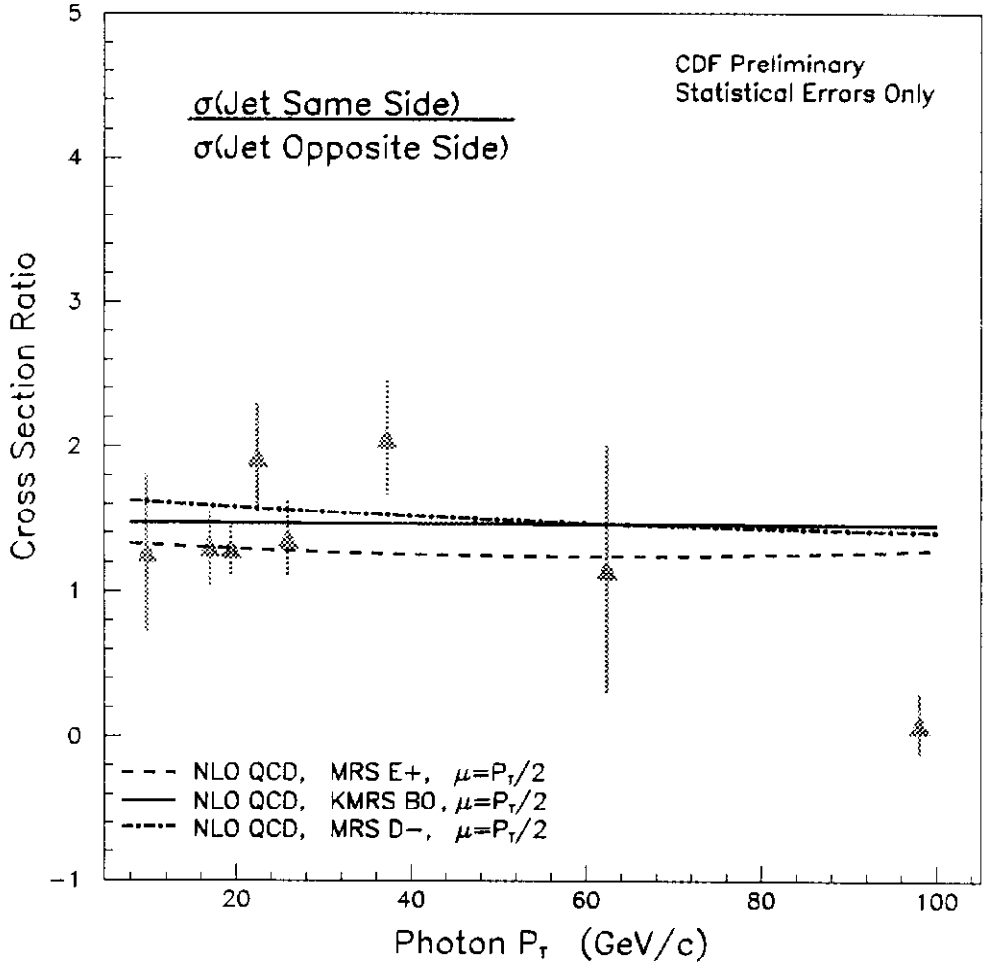

Figure 14: The ratio of two photon+jet cross sections is shown. This is the ratio of the case when the jet and photon are on the same side of the detector (in pseudorapidity) to the case when the jet is on the opposite side from the photon.